Complete-velocity-range description of negative-ion conversion of neutral atoms on an alkali-metal-halide surface under grazing geometry

Hu Zhou,[1,*] Wang Zhou,[1] Meixiao Zhang,[1] Lihua Zhou,[1] Yulong Ma,[1] Guangyi Wang,[1] Yong Wu,[2] Bowen Li,[1] and Ximeng Chen[1,*]

[1]*School of Nuclear Science and Technology, Lanzhou University, Lanzhou 730000, China*

[2]*Key Laboratory of Computational Physics, Institute of Applied Physics and Computational Mathematics, Beijing 100088, China*

(Received 8 April 2016; revised manuscript received 24 May 2016; published 27 June 2016)

We propose a simple theoretical approach to consider negative-ion conversion of neutral atoms grazing on alkali-metal-halide crystal surfaces over the complete velocity range. The conversion process is viewed as a series of successive binary collisions between the projectile and the negatively charged sites on the surface along their trajectories due to localization of valence-band electrons at the anionic sites of the crystal. Conversion from F^0 to F^- via grazing scattering in LiF(100) and KI(100) is demonstrated with this model, which incorporates the key factors of image interaction and Mott-Littleton polarization interaction for electron capture. It also incorporates the decrease in the electron affinity due to Coulomb barrier tunneling of large-velocity negative ions to the vacuum level near surface anion sites. The pronounced differences in the efficiency of F^- formation at LiF(100) and KI(100) surfaces are well explained by the proposed model. The relative efficiency and related saturation of the negative-ion formation for LiF and KI crystals compare well with experimental results.

DOI: 10.1103/PhysRevA.93.062708

I. INTRODUCTION

Charged-particle–surface interaction processes play an important role in many technological fields such as (1) semiconductor miniaturization and the production of self-assembled nanodevices; (2) analysis, characterization, and manipulation of surfaces [1,2]; and (3) microfabrication based on reactive-ion etching and ion lithography [3]. In those applications, charge transfer between an ion and a surface is a crucial intermediate step. Furthermore, the final charge state of the scattered, sputtered, or recoiled ions is primarily attributed to the charge-transfer process. It is therefore closely related to the improvement of various analytical techniques and the production of ion beams; representative examples include low-energy-ion scattering spectroscopy, secondary-ion mass spectrometry, and metastable-atom deexcitation spectroscopy [4].

For metal surfaces, the mechanism of charge exchange is well understood [5]; by contrast, for insulator and semiconductor surfaces, although there have been several studies regarding electron emission [6], electron excitation [7], energy loss [8], surface nanostructure [9], and electron-transfer [10] processes, the related negative-ion conversion mechanism has apparently not yet been adequately explored. One typical example of a mechanism that requires study is the unexpectedly high fraction of negative-ion conversion for atoms in grazing scattering on ionic crystal surfaces [11].

The motivation for the present study is to address the following deficiencies of previous theoretical treatments: (1) although *ab initio* quantum chemistry parameter-free theoretical calculations [12] can reproduce the low-velocity part of the experimental data (including the velocity thresholds for negative-ion formation) quite well, those calculations are very complicated; and (2) the existing theoretical treatment fails to reproduce the experimental data at high velocities because it does not consider the possible electron-loss processes that can lead to the destruction of the formed negative ion. Therefore, further studies that consider high-velocity negative-ion destruction are required.

In this paper, we demonstrate a simple general approach to consider the complete velocity range of negative-ion formation in grazing scattering from any AB-type ionic crystal surface (alkali-metal halides and oxides). We assess this model by considering both LiF(100) and KI(100) surface systems for the following reasons:

(1) Experimental data are available regarding the yields of F^- ions in grazing scattering of F^0 atoms from LiF(100) and KI(100) surfaces [11].

(2) A parameter-free study of F^- formation has been done using a model based on a series of binary collisions and the "localized hole" approximation [12]; that model provides a basis for comparison in the present study.

(3) Because of the different electronic structures of the valence and conduction bands of the two insulators, we can expect additional information regarding charge transfer of atom-insulator interactions.

The present paper is organized as follows. Section II presents the basic mechanism that governs the electron-transfer process. Section III describes the calculation details of the key features of the energy difference (energy defect) in the electron capture mechanism: we first discuss the nonpolarization point-charge energy defect of electron capture in Sec. III A. Section III B is devoted to the treatment of the MottLittleton (ML) polarization interaction in electron capture, and in Sec. III C we determine the image interaction contribution to the electron capture. We present the results of our conversion calculation in Sec. IV. Initially, in Sec. IV A, we model the energy defect that incorporates both polarization corrections of the ML polarization and image interaction contributions. Section IV B presents and discusses the single-collision negative-ion conversion in detail. In Sec. IV C, we compare the theoretical calculation with the available

*zhouhu19860224@163.com and chenxm@lzu.edu.cn

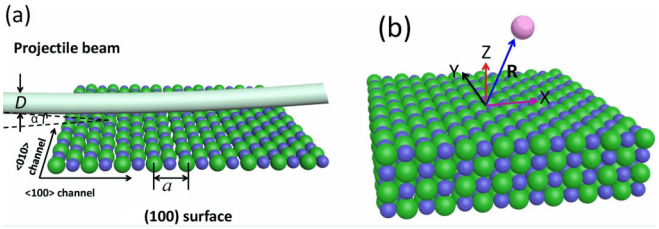

FIG. 1. (a) Sketch of an $A^0_{\rm gas}$ projectile undergoing grazing scattering from an ionic-crystal surface [here, LiF(100) or KI(100)], where α and D are the incident angle and the diameter of the beam, respectively. The direction of the beam is parallel to the $\langle 100\rangle$ surface axis channel. (b) Sketch of the $\{A^0_{\rm gas} - X^-_{\rm active\ site}\}$ binary-collision system on the surface, which consists of {899 point charges + $X^-_{\rm active\ site}$} organized in four layers.

experimental measurements for a range of velocity fields. The conclusions are presented in Sec. V. We use atomic units throughout this paper, unless otherwise specified.

II. THEORETICAL MODELS

The alkali-metal-halide ionic crystal has alternating $+1$ and -1 charges distributed at the lattice sites of M^+ and X^-, where M is the metal and X the halogen, respectively. For neutral $A^0_{\rm gas}$ projectiles undergoing grazing scattering along the $\langle 100\rangle$ direction of LiF(100) and KI(100) surfaces shown in Fig. 1(a), the trajectories result from small-angle scattering events of projectiles with many ions in the surface plane and are nearly identical for all projectiles [13]. The valence band of the alkali-metal halide originates from the $X^-(np_{x,y,z})$ orbitals, and the valence-band electrons are localized at the X^- sites [14]. Electron capture of a projectile $A^0_{\rm gas}$ from the surface of an alkali-metal-halide ionic crystal is closely related to the localized valence-band electrons. Therefore, a series of sequentially binary collisions of a projectile with X^- ions at the crystal surface treatment is considered here [12,15]:

$$A^0_{\rm gas} + X^-_{\rm active\ site} \rightarrow A^-_{\rm gas} + X^0_{\rm active\ site}. \tag{1}$$

In Eq. (1), "active site" specifies the site that actually participates in the charge-transfer process and is considered to be at the origin of the frame. Other ions of the crystal are spectators and considered as point charges. A key feature that determines the efficiency of the electron-capture mechanism is the energy difference (hereafter referred to as the "energy defect") between the initial $(A^0_{\rm gas} + X^-_{\rm active\ site})$ and final $(A^-_{\rm gas} + X^0_{\rm active\ site})$ diabatic states during the collision and is given by

$$\Delta E(\mathbf{R},v) = E\left(A^-_{\rm gas} + X^0_{\rm active\ site}\right) - E\left(A^0_{\rm gas} + X^-_{\rm active\ site}\right), \tag{2}$$

where $\Delta E(\mathbf{R},v)$ is the energy required to move an electron from the valence band near the $X^-_{\rm active\ site}$ at the surface to the projectile affinity level located at $\mathbf{R}$.

The closest-approach distance of the projectile $Z_{\rm tp}^{A^0_{\rm gas}}$ $(2.0 \leqslant Z_{\rm tp}^{F^0_{\rm gas}} \leqslant 4.0$ a.u. (where "tp" indicates the turning point) for F-LiF(100) and KI(100) [12]) to the surface is greater than the radius of the projectile $r_{A^0_{\rm gas}}$ ($r_{F^0_{\rm gas}} \approx 1.0$ a.u. [16]), thereby significantly avoiding overlap of the electronic clouds of the $X^-_{\rm active\ site}$ with the projectile and leading to the following equation:

$$E\left(A^0_{\rm gas} + X^-_{\rm active\ site}\right) = E_{X^-_{\rm active\ site}} + E_{A^0_{\rm gas}} + \frac{1}{2}\sum_{i\neq j}\frac{q_i q_j}{|\mathbf{r}_i - \mathbf{r}_j|} - \sum_i \frac{q_i}{|\mathbf{r}_i|}, \tag{3}$$

where the summations run over all point charges that exclude the $X^-_{\rm active\ site}$. $E_{X^-_{\rm active\ site}}$ and $E_{A^0_{\rm gas}}$ are the total energies of the free $X^-_{\rm active\ site}$ ion and neutral projectile $A^0_{\rm gas}$, respectively. The $q_i = \pm 1$ are the point charges at the crystal sites located at $\mathbf{r}_i$ with respect to the active site. The third term gives the interaction energy between the point charges. The last term is the interaction energy between the active site (having a charge of -1) and all other sites of the crystal [17].

Similarly,

$$E\left(A^-_{\rm gas} + X^0_{\rm active\ site}\right) = E_{X^0_{\rm active\ site}} + E_{A^-_{\rm gas}} + \frac{1}{2}\sum_{i\neq j}\frac{q_i q_j}{|\mathbf{r}_i - \mathbf{r}_j|} - \sum_i \frac{q_i}{|\mathbf{R} - \mathbf{r}_i|} + P_{\rm ML}(\mathbf{R}) + U_{\rm image}(\mathbf{R},v), \tag{4}$$

where $P_{\rm ML}(\mathbf{R})$ is the ML polarization interaction [18]. The last term $U_{\rm image}(\mathbf{R},v)$ is the image interaction, which originates from the formed negative ions interacting with their own image charge created by the field polarization of the insulating surface in the final state of electron capture [19].

Combining Eqs. (2), (3), and (4), one obtains the energy defect

$$\Delta E(\mathbf{R},v) = \varepsilon_{X^-_{\rm active\ site}} - \varepsilon_{A^-_{\rm gas}} + \left\{\sum_i \frac{q_i}{|\mathbf{r}_i|} - \sum_i \frac{q_i}{|\mathbf{R} - \mathbf{r}_i|}\right\} + P_{\rm ML}(\mathbf{R}) + U_{\rm image}(\mathbf{R},v), \tag{5}$$

where $\varepsilon_{X^-_{\rm active\ site}} = E_{X^0_{\rm active\ site}} - E_{X^-_{\rm active\ site}}$, and $\varepsilon_{A^-_{\rm gas}} = E_{A^0_{\rm gas}} - E_{A^-_{\rm gas}}$ gives the binding energies of the electron in the free $X^-_{\rm active\ site}$ ion and the free $A^-_{\rm gas}$ ($\varepsilon_{F^-_{\rm gas}} = 3.4$ eV [11]). The terms in the braces correspond to the difference between the Madelung potential created by the point charges at the $X^-_{\rm active\ site}$ and that at the point $\mathbf{R}$. $\mathbf{R} = \{X,Y,Z\}$ represents the position vector of the projectile relative to the $X^-_{\rm active\ site}$, as shown in Fig. 1(b).

III. CALCULATION DETAILS

A. Nonpolarized point-charge energy defect

From Eq. (5), one can obtain the nonpolarized point-charge energy defect, $\Delta E_{\rm PC}(\mathbf{R}) = \varepsilon_{X^-_{\rm active\ site}} - \varepsilon_{A^-_{\rm gas}} + \{\sum_i \frac{q_i}{|\mathbf{r}_i|} - \sum_i \frac{q_i}{|\mathbf{R}-\mathbf{r}_i|}\}$. For the studied $F^0_{\rm gas}$-LiF(100) and KI(100) systems, we used {899 point charges + $X^-_{\rm active\ site}$} and organized them into four parallel layers, where the origin was attached to the surface $X^-_{\rm active\ site}$ shown in Fig. 1(b); this approach guaranteed the accuracy of the calculated Madelung potential on the active site to be better than 5×10^{-4} eV

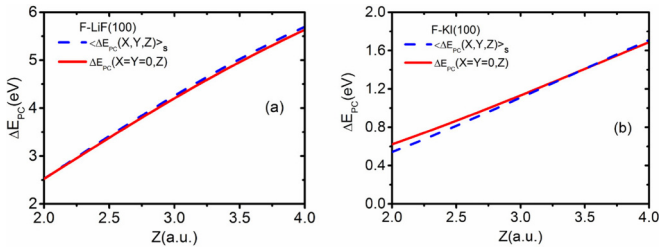

FIG. 2. (a) Both $\langle \Delta E_{PC}(X,Y,Z)\rangle_S$ and $\Delta E_{PC}(X=Y=0,Z)$ as functions of surface altitude Z for the F^0_{gas}-LiF(100) surface. (b) Similar to (a), but for the F^0_{gas}-KI(100) case.

[12,15]. Considering the scales of incident A^0_{gas} and surface $X^-_{active\ site}$, if all the incident projectiles impacted the effective $X^-_{active\ site}$ area of $\boldsymbol{S} = \{-a/4 \leqslant X \leqslant a/4, -a/4 \leqslant Y \leqslant a/4\}$ (a is the lattice constant), then there would always be several projectiles in the area of $\boldsymbol{S}_0 = \{-(\frac{a}{4} - r_{A^0_{gas}}) \leqslant X \leqslant (\frac{a}{4} - r_{A^0_{gas}}), -(\frac{a}{4} - r_{A^0_{gas}}) \leqslant Y \leqslant (\frac{a}{4} - r_{A^0_{gas}})\}$. Therefore, the actual reaction energy defect in the $X^-_{active\ site}$ scale of $\boldsymbol{S}$ was the energy defect in $\boldsymbol{S}_0$. Next, we calculated $\langle \Delta E_{PC}(X,Y,Z)\rangle_{S_0} = (1/S_0)\iint_{S_0} \Delta E_{PC}(X,Y,Z)dXdY$ and $\Delta E_{PC}(X=0,Y=0,Z)$; the calculation results are shown in Fig. 2 . The negligible difference clearly justifies the approximation of ΔE_{PC} in $\boldsymbol{S}$ by $\Delta E_{PC}(X=0,Y=0,Z)$.

B. ML polarization effect

Upon electron capture, the projectile (here, F^-_{gas}) had a charge of -1. Simultaneously, a hole with a charge of $+1$ was created at the active site of the previously neutral crystal surface, which resulted in an effective $\oplus - \Theta$ dipole, whose $+1$ and -1 charges are located at $\mathbf{R}_+ = \mathbf{0}$ and $\mathbf{R}_- = \mathbf{R}$, respectively. The field of the dipole polarized the lattice ions (treated as merely point charges) and introduced a field-induced dipole contribution of the ML polarization interaction to the energy of the final $(A^-_{gas} + X^0_{active\ site})$ state as follows [17,20]:

$$P_{ML}(\mathbf{R}) = -\frac{\alpha_\pm}{2}\sum_{i_\pm}\left\{\frac{\mathbf{r}_{i_\pm} - \mathbf{R}_+}{|\mathbf{r}_{i_\pm} - \mathbf{R}_+|^3} - \frac{\mathbf{r}_{i_\pm} - \mathbf{R}_-}{|\mathbf{r}_{i_\pm} - \mathbf{R}_-|^3}\right\}^2, \quad (6)$$

where i runs over all lattice sites $\mathbf{r}_i$ except the active one; the M^+ (Li^+ or K^+) and X^- (F^- or I^-) ion polarizations taken from [21] are $\alpha_+ = 0.2027$ a.u. and $\alpha_- = 4.3233$ a.u., respectively, for LiF and $\alpha_+ = 8.9604$ a.u. and $\alpha_- = 43.1967$ a.u., respectively, for KI. In principle, we should calculate $P_{ML}(\mathbf{R})$ at the $X^-_{active\ site}$ effective scale of $\boldsymbol{S}$. Because of symmetry $[P_{ML}(-X,Y,Z) = P_{ML}(X,-Y,Z) = P_{ML}(X,Y,Z)]$, the results for only $P_{ML}(\mathbf{R})$ in the area of $\{0 \leqslant X \leqslant a/4, 0 \leqslant Y \leqslant a/4\}$ at different altitudes ($Z = 3.0$, 3.5, 4.0, and 4.5 a.u.) are presented in Figs. 3(a)–3(d) for KI. The figures show that $-1.2 \leqslant P_{ML}(\mathbf{R}) \leqslant -0.4$ eV for Z from 3.0 a.u. to 4.5 a.u. Taking the average of $P_{ML}(\mathbf{R})$ over X, Y in $\boldsymbol{S}$, that is, $\langle P_{ML}(X,Y,Z)\rangle_S = (1/S)\iint_S P_{ML}(X,Y,Z)dXdY$, we obtain -1.1 eV $\leqslant \langle P_{ML}(X,Y,Z)\rangle_S \leqslant -0.6$ eV for Z from 3.0 to 4.5 a.u., which is significantly greater than the range of -0.38 eV $\leqslant \langle P_{ML}(X,Y,Z)\rangle_S \leqslant -0.26$ eV for LiF.

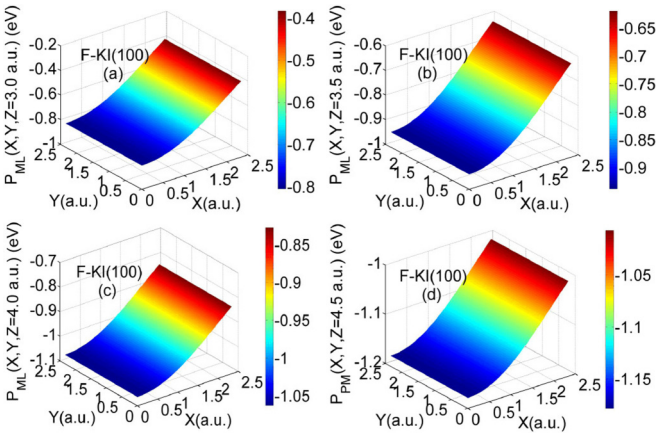

FIG. 3. (a), (b), (c), and (d) show the ML polarization contributions $P_{ML}(\mathbf{R})$ of F-KI(100) within the surface X^-_{site} (here I^-_{site}) scale $\boldsymbol{S}$ at projectile-surface altitudes of $Z = 3.0$, 3.5, 4.0, and 4.5 a.u., respectively.

C. Image interaction effect

The formed negatively charged projectile (F^-_{gas}) interacts with its own image created by field polarization of the crystal [19]. This image interaction occurs in the final $(A^-_{gas} + X^0_{active\ site})$ state. For a particle with charge Q (here, -1) moving with a velocity parallel component $v_{//} = v\sin\alpha$ to the surface, according to the surface response formalism presented in Ref. [22], one obtains

$$U_{image}(Z,v_{//}) = -\frac{Q}{\pi v_{//}}\int_0^\infty d\omega K_0\left(\frac{2\omega Z}{v_{//}}\right)\mathrm{Re}\left(\frac{\varepsilon(\omega)-1}{\varepsilon(\omega)+1}\right), \quad (7)$$

where K_0 is the second-type modified Bessel function of order 0. We used the surface response function $[\varepsilon(\omega)-1]/[\varepsilon(\omega)+1]$ with the dielectric constant $\varepsilon(\omega)$ of an insulator crystal. A two-oscillator model was introduced to obtain the dielectric constant for both LiF and KI crystals as follows [23]:

$$\varepsilon_1(\omega) = \varepsilon_\infty + \sum_{i=1}^{2}\frac{4\pi\rho_i\omega_i^2(\omega_i^2-\omega^2)}{(\omega_i^2-\omega^2)^2+(\gamma_i\omega)^2},$$
$$\varepsilon_2(\omega) = \sum_{i=1}^{2}\frac{4\pi\rho_i\omega\gamma_i\omega_i^2}{(\omega_i^2-\omega^2)^2+(\gamma_i\omega)^2}. \quad (8)$$

Because $\varepsilon(\omega) = \varepsilon_1(\omega) + i\varepsilon(\omega)$, we obtain

$$\mathrm{Re}\left(\frac{\varepsilon(\omega)-1}{\varepsilon(\omega)+1}\right) = \frac{\varepsilon_1^2(\omega)+\varepsilon_2^2(\omega)-1^2}{(\varepsilon_1(\omega)+1)^2+\varepsilon_2^2(\omega)}. \quad (9)$$

The parameters $\varepsilon_\infty = 1.96$, $\omega_1 = 307.5\ cm^{-1}$, $\omega_2 = 501.4\ cm^{-1}$, $4\pi\rho_1 = 6.67$, $4\pi\rho_2 = 0.116$, $\gamma_1/\omega_1 = 0.057$, and $\gamma_2/\omega_2 = 0.173$ for LiF and $\varepsilon_\infty = 2.7$, $\omega_1 = 102\ cm^{-1}$, $\omega_2 = 316\ cm^{-1}$, $4\pi\rho_1 = 2.136$, $4\pi\rho_2 = 0.276$, $\gamma_1/\omega_1 = 0.084$, and $\gamma_2/\omega_2 = 0.3$ for KI can be obtained from [23].

From Eqs. (7)–(9), the calculated image interaction as a function of the projectile's incident velocity v and surface altitude Z for both F^0_{gas}-LiF(100) and KI(100) collision systems are displayed in Figs. 4(a) and 4(c), respectively.

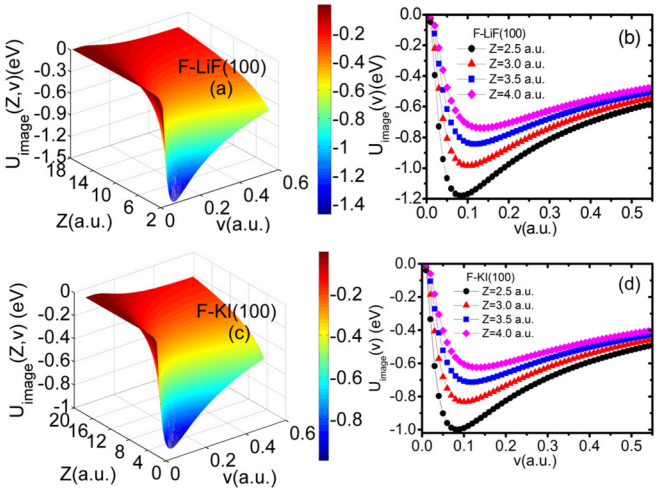

FIG. 4. (a) Three-dimensional (3D) plot of U_{image} as a function of both surface altitude Z and projectile velocity v. (b) U_{image} as a function of projectile velocity v for fixed surface altitudes of $Z = 2.5$, 3.0, 3.5, and 4.0 a.u. (c) and (d) are similar to (a) and (b), respectively, but for the F-KI(100) case.

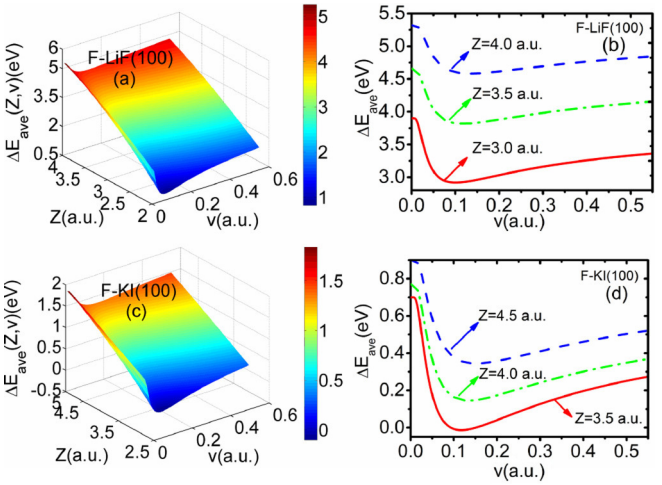

FIG. 5. (a),(c) Computed average energy defects $\Delta E_{\text{ave}}(Z,v)$ on the scale $\boldsymbol{S}$ of the surface $X^-_{\text{active site}}$ (F^- or I^-) as a function of the surface altitude Z and projectile velocity v for the F^0_{gas}-LiF(100) and KI(100) cases, respectively. (b) $\Delta E_{\text{ave}}(Z,v)$ as a function of the projectile velocity v for fixed surface altitudes of $Z = 3.0$, 3.5, and 4.0 a.u. for the F^0_{gas}-LiF(100) case. (d) $\Delta E_{\text{ave}}(Z,v)$ as a function of the projectile velocity v for fixed surface altitudes of $Z = 3.5$, 4.0, and 4.5 a.u. for the F^0_{gas}-KI(100) case.

For $v < 0.08$ a.u., the small vertical energy component $E_\perp$ ($E_\perp < 0.9$ eV) meant that the projectile could not reach the surface altitude range of 2.5 a.u. $\leqslant Z \leqslant$ 4.0 a.u. Therefore, the image interaction model in this work is suitable in the velocity range of $v \geqslant 0.08$ a.u. Figures 4(b) and 4(c) present the projection of $U_{\text{image}}(Z,v)$ for four different surface altitudes of $Z = 2.5$,3.0,3.5, and 4.0 a.u. for both cases. The magnitude of the image interaction $U_{\text{image}}(Z,v)$ was observed to decrease with increasing Z and increase with decreasing projectile velocity v within the focused $v \geqslant 0.08$ a.u velocity range.

IV. RESULTS AND DISCUSSION

A. Electron-capture energy defect

Incorporating both of the key factors of ML polarization and image interaction discussed above, one can obtain the average energy defect $\Delta E_{\text{av}}(Z,v)$ on the scale $\boldsymbol{S}$ of a surface $X^-_{\text{active site}}$ (F^- or I^-):

$$\begin{aligned}\Delta E_{\text{ave}}(Z,v) &= \langle \Delta E_{\text{PC}}(X,Y,Z)\rangle_{\boldsymbol{S}} \\ &\quad + \langle P_{\text{ML}}(X,Y,Z)\rangle_{\boldsymbol{S}} + U_{\text{image}}(Z,v) \\ &\approx \Delta E_{\text{PC}}(X=Y=0,Z) + \langle P_{\text{ML}}(X,Y,Z)\rangle_{\boldsymbol{S}} \\ &\quad + U_{\text{image}}(Z,v), \end{aligned} \tag{10}$$

where $\langle \Delta E_{\text{PC}}(X,Y,Z)\rangle_{\boldsymbol{S}}$ is the average nonpolarized point-charge energy defect, $\langle P_{\text{ML}}(X,Y,Z)\rangle_{\boldsymbol{S}}$ is the average ML polarization interaction, and $U_{\text{image}}(Z,v)$ is the image interaction. Figures 5(a)–5(d) show the computational results obtained using Eq. (10).

The energy differences $\Delta E_{\text{ave}}(Z,v)$ for electron transfer in the F^0_{gas}-LiF(100) and F^0_{gas}-KI(100) systems are shown in Figs. 5(a) and 5(b) and Figs. 5(c) and 5(d), respectively. A characteristic of the electron-transfer energy defect $\Delta E_{\text{ave}}(Z,v)$ was its rapid increase with Z. This characteristic is well illustrated in Figs. 5(b) and 5(d), where the results for different Z values for F^0_{gas}-LiF(100) and F^0_{gas}-KI(100), respectively, are presented.

The smaller $\Delta E_{\text{ave}}(Z,v)$ energy differences in the F^0_{gas}-KI(100) case than in the F^0_{gas}-LiF(100) case arose from the following factors: (1) The lattice constant of the KI crystal ($a = 13.34$ a.u. [11]) was almost twice as large as that of LiF ($a = 7.592$ a.u. [11]). From Eq. (5), the energy difference $\Delta E_{\text{PC}}(\mathbf{R})$ was governed by the difference between the Madelung potentials at the active sites and at the position $\mathbf{R}$ of the projectile. Because the characteristic size of the variation of the Madelung field is given by the lattice constant a, the smaller the ratio R/a, the smaller the difference in the braces and consequently the smaller the contribution of $\Delta E_{\text{PC}}(\mathbf{R})$ [see Fig. 2(b)] to $\Delta E(\mathbf{R},v)$. (2) Compared with the LiF crystal, the large anion and cation polarizations [$\alpha_{I^-} \approx 10\alpha_{F^-}, \alpha_{K^+} \approx 45\alpha_{Li^+}$] for the KI case led to a large ML polarization reduction [see Figs. 3(a)–3(d) and the related discussion] in $\Delta E_{\text{ave}}(Z,v)$. (3) $\varepsilon_{X^-_{\text{active site}}} - \varepsilon_{A^-_{\text{gas}}} = 0$ for the F^0_{gas}-LiF(100) case, whereas it was equal to -0.07 eV for the F^0_{gas}-KI(100) case. Note that despite the substantial image interaction reducing $U_{\text{image}}(Z,v)$ [e.g., -1.0 eV $\leqslant U_{\text{image}}(Z = 3.0$ a.u., $v \geqslant 0.08$ a.u.$) \leqslant -0.6$ eV for F^0_{gas}-LiF and $-0.85 \leqslant U_{\text{image}}(Z = 3.0$ a.u., $v \geqslant 0.08$ a.u.$) \leqslant -0.43$ eV for F^0_{gas}-KI, (see Fig. 4)] to the energy defect $\Delta E_{\text{ave}}(Z,v)$, the equivalent magnitude [$\Delta U_{\text{image}}(Z = 2.5,3.0,3.5,4.0$ a.u.;$v \geqslant 0.08$ a.u.$) \leqslant 0.2$ eV between $F^0_{\text{gas}} -$ LiF and $F^0_{\text{gas}} -$ KI] indicates that this effect is not responsible for the energy defect difference between both cases. However, the observed projectile velocity dependence of $\Delta E_{\text{av}}(Z,v)$ solely originated from the image interaction.

For F^0_{gas}-KI(100), $\Delta E_{\text{ave}}(Z,v)$ was observed to pass through zero for trajectories with surface distances of $Z < 3.5$ a.u. [Fig. 5(c)]. This feature indicated that the Landau-Zener

curve-crossing mechanism [24] is appropriate for treating F^0_{gas}-KI(100) electron transfer at such small distances. A detailed discussion of that mechanism is beyond the scope of the present study. However, note that the existence of this potential-energy surface crossing in F^0_{gas}-KI(100) also implies that electron transfer is easier in this system than in F^0_{gas}-LiF(100), in which higher energies are required to overcome the larger energy defect [approximately 2 to 5 eV, Figs. 5(a) and 5(b)].

B. Single-collision negative-ion conversion

1. Electron loss

In Ref. [25], Borisov and Gauyacq proved that short-range binary-type H^--F^-_{site} interactions are responsible for electron detachment and result in electron emission into the vacuum. Therefore, here we considered the Coulomb repulsive barrier tunneled to the vacuum level as a result of the weak electron affinity of the negative ions formed during the interaction with the surface X^-. Consider the following two conditions of the present treatment: (1) X^-(F^- or I^-) was fixed at the surface and could be assumed to have an infinite mass and (2) the effective interaction distance was due to the projectile vertical energy component $E_\perp$ with the projectile atomic mass M and incidence angle α relative to the surface plane. Both of these two conditions led to a complete equivalence between the present F^--X^- and the gas-phase e^--F^- collision for the electron affinity tunneling process, in which the effective projectile electron with energy of $E_\perp$ and F^- is fixed. Therefore, as in Ref. [26], the detachment probability of the formed negative ions can be expressed as in [27]:

$$P_{\rm det}(E_\perp) = \exp[-2\Gamma(E_\perp)]. \tag{11}$$

The Hamiltonian of the effective projectile electron can be expressed as in [28]:

$$H = P^2/2 + 1/R. \tag{12}$$

Here, simply take the nonscreened Coulomb potential $1/R$; see Fig. 6(a). For each energy $E_\perp = H$, the tunneling action that enters into Eq. (11) can be calculated from the imaginary momentum $p = (-P^2)^{1/2}$ of Eq. (12) by

$$\Gamma = \int_{R_1}^{R_2} p\,dR. \tag{13}$$

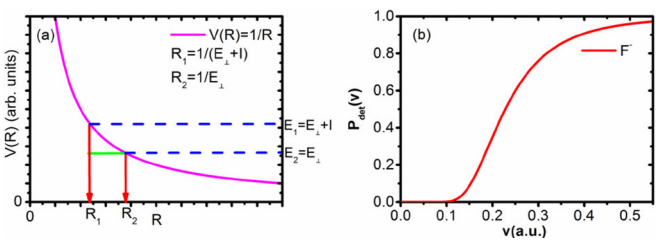

FIG. 6. (a) Tunneling dynamics for the potential $V(R) = 1/R$. The classically allowed incoming and outgoing trajectories with the energies E_1 and E_2, respectively, are indicated by the blue dashed lines, and the tunneling part is indicated by the green solid line. (b) Tunneling detachment probabilities for $F^- + F^-_{site} \to F^0 + e^- + F^-_{site}$ and $F^- + I^-_{site} \to F^0 + e^- + I^-_{site}$ were calculated using Eq. (11).

The integration limits are the outer turning point of R_2 where the orbit becomes classically allowed [$p(R_2) = 0, R_2 = 1/E_\perp$], and a starting point R_1; see Fig. 6(a).

The small tunneling probability which determines the threshold detachment according to Eq. (11) close to $E_\perp = 0$ is too crude. Here, considering that the projectile is repelled by the loosely bound affinity electron, it will not reach $R_1 = 0$ at low impact energy of $E_\perp$. Actually, one can approximate R_1 by the classical turning point of the effective incoming electron. This turning point of the incoming electron can be obtained by putting $P = 0$ in Eq. (12) at the incoming effective electron energy of $E_1 = E_\perp + I$ [I is the binding energy of the loosely bound affinity electron of the projectile A^-_{gas} ($I = \varepsilon_{A^-_{gas}}$)], which yields $R_1 = 1/(E_\perp + I)$. The outgoing electron pair has an initial momentum of $p(R_1) = \sqrt{2I}$ and follows the Hamiltonian of Eq. (12) on the final energy surface $E_1 = E_\perp$. The calculated tunneling detachment probabilities for $F^- + F^-_{site} \to F^0 + e^- + F^-_{site}$ and $F^- + I^-_{site} \to F^0 + e^- + I^-_{site}$ from Eqs. (11)–(13) were

$$P_{\rm det}(E_\perp) = \exp\left[-\frac{2\sqrt{2}}{\sqrt{E_\perp}}\left(\arctan\sqrt{\frac{I}{E_\perp}} - \frac{\sqrt{IE_\perp}}{I+E_\perp}\right)\right]$$

and are displayed in Fig. 6(b). Obviously, one can observe a large increase after a velocity threshold of $v^{\rm loss}_{\rm th} \approx 0.1$ a.u.

2. Binary-collision negative-ion conversion

For single-collision negative-ion conversion of the incident atom with the surface $X^-_{\rm active\ site}$, considering the trajectory statistics, the final probability of negative-ion conversion can be described by $P^{\rm site}_{\rm sin}(Z,v) = 2P^{\rm site}_{\rm cap}(Z,v)[1 - P_{\rm det}(v)]$, where the electron capture probability $P^{\rm site}_{\rm cap}(Z,v)$ for neutral projectiles from the surface $X^-_{\rm active\ site}$ was obtained from Ref. [11] with the present energy defect of Eq. (10). In fact, $P^{\rm site}_{\rm sin}(Z,v)$ represents the negative-ion conversion probability of a neutral projectile lying in the (X, Y) plane at a distance Z from the surface. If $N_{\rm proj}$ and D represent the total number of projectiles and the size of the projectile beam, respectively [see Fig. 1(a)], then $N_{\rm proj}/[D/(a/2)]$ is the number of projectiles per active site with effective size $a/2$ for $X^-_{\rm active\ site}$ at the surface. Thus, the number of negative ions formed per active site can be expressed as

$$\frac{N_{\rm proj}}{D/(a/2)} P^{\rm site}_{\rm sin}(Z,v).$$

Because there are D/a active sites in the direction [$\langle 010\rangle$ axis channel] normal to the beam's direction of travel [$\langle 100\rangle$ axis channel], the total number of negative ions N^- is given by $N^- = \frac{1}{2}N_{\rm proj}P^{\rm site}_{\rm sin}(Z,v)$. Thus, the negative-ion conversion probability for crossing a row of surface ions oriented along the $\langle 010\rangle$ channeling direction is $P^{\rm row}_{\rm sin}(Z,v) = \frac{1}{2}P^{\rm site}_{\rm sin}(Z,v)$.

Figures 7(a) and 7(b) display the Z and v dependences of computed $P^{\rm site}_{\rm sin}(Z,v)$ probabilities for the F^0_{gas}-LiF(100) case. The figures show that, for small velocities, transitions occurred only for trajectories that passed close to the $X^-_{\rm active\ site}$ (small Z). This $\Delta E_{\rm ave}(Z,v)$ result was because the energy difference between final and initial states $\Delta E_{\rm ave}(Z,v)$ was smallest for those trajectories (Fig. 5). The increase in $\Delta E_{\rm ave}(Z,v)$ strongly

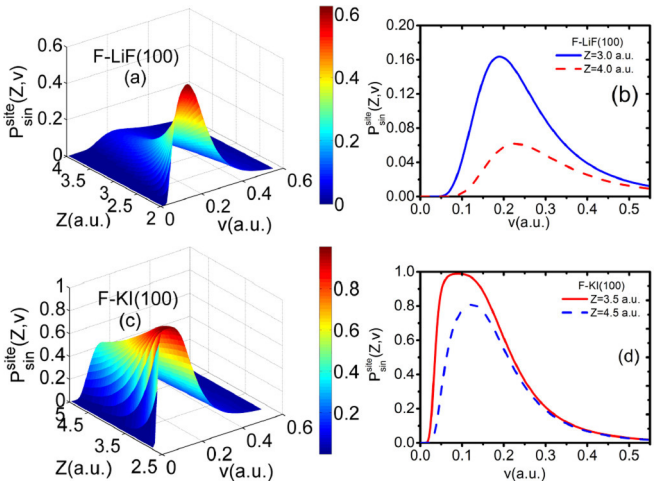

FIG. 7. (a) Probability of negative-ion conversion for a collisional F^0_{gas} with an $F^-_{active\ site}$ at the LiF(100) surface in a single binary collision: $F^0_{gas} + F^-_{active\ site} \rightarrow F^-_{gas} + F^0_{active\ site}$. The calculation was made within the effective region $\boldsymbol{S}$ of $F^-_{active\ site}$ at the LiF(100) surface. The figure displays, as a perspective view, the dependences of the probability $P^{site}_{sin}(Z,v)$ on the projectile velocity v and the surface altitude Z. (b) Projectile velocity dependence of the negative-ion conversion probability [$P^{site}_{sin}(Z,v)$] in a single binary collision. Two representative values, $Z = 3.0$ a.u. (blue solid line) and 4.0 a.u. (red dashed line), of the surface altitude are displayed. (c) and (d) are similar to (a) and (b) respectively, but for the case of a single binary collision of $F^0_{gas} + I^-_{active\ site} \rightarrow F^-_{gas} + I^0_{active\ site}$ and surface altitudes of $Z = 3.5$ and 4.5 a.u.

suppressed transitions for large values of the altitude Z. The increase in collision velocity can clearly activate the transitions for large Z.

A comparison of Figs. 7(b) and 7(d) indicates that an increase in the altitude Z led to substantial reductions in the electron-transfer probabilities. Figures 5(a)–5(d) also indicate that this behavior was a result of the increase in $\Delta E_{ave}(Z,v)$ when Z increased. As a result, the region with small projectile-surface altitudes Z contributed the most to the negative-ion population.

Figures. 7(c) and 7(d) display the Z and v dependences of the computed $P^{site}_{sin}(Z,v)$ probabilities for the F^0_{gas}-KI(100) case. Remarkable differences compared with the F^0_{gas}-LiF(100) case [Figs. 7(a) and 7(b)] can be seen. These differences are particularly striking in the comparison of the commensurate distances of $Z = 3.0$ a.u. and 3.5 a.u. from the LiF(100) and KI(100) surfaces shown in Figs. 7(b) and 7(d): in the F^0_{gas}-KI(100) case, the transition probability is much higher, and there is a negligible velocity threshold for negative-ion formation. Note that this comparison is relevant because the important turning-point region of the F^0_{gas} projectile in the two cases is 2.0 a.u. $\leqslant Z_{tp} \leqslant$ 4.0 a.u. [12]; this range corresponds to the energies at which rapid onsets of negative-ion formation were observed.

The more efficient negative-ion formation in F^0_{gas}-KI(100) than in F^0_{gas}-LiF(100) clearly occurred because of the small energy difference $\Delta E_{ave}(Z,v)$ in F^0_{gas}-KI(100). This feature was primarily due to both the large lattice constant of KI, which led to a small $\Delta E_{PC}(\mathbf{R})$ (as discussed in Sec. IV A), and the large ML-polarization-induced reduction in $\Delta E(\mathbf{R},v)$. As shown in Figs. 7(b) and 7(d), the $P^{site}_{sin}(Z = 3.5$ a.u., $v)$ and $P^{site}_{sin}(Z = 4.5$ a.u., $v)$ results for F^0_{gas}-KI(100) are indeed significantly greater than the $P^{site}_{sin}(Z = 3.0$ a.u., $v)$ and $P^{site}_{sin}(Z = 4.0$ a.u., $v)$ results for F^0_{gas}-LiF(100).

An important feature of the results shown in Figs. 7(a)–7(d) is that in the investigated velocity range (especially at the low velocities, which corresponded to sharp onsets of negative-ion conversion), the electron-transfer transitions were well localized within the surface X^-_{site} scale of $\boldsymbol{S}$. This localization causes one to expect that the electron-transfer regions correspond to the different nonoverlapping X^- sites. This result provides strong support for the binary-type collision treatment used in the present work.

The results for the negative-ion conversion probability per $X^-_{active\ site}$ $P^{site}_{sin}(Z,v)$ are displayed in Figs. 7(b) and 7(d) for the cases of F^0_{gas}-LiF(100) and F^0_{gas}-KI(100), respectively. In both cases, increasing the surface altitude Z appeared to reduce the electron-transfer probability and shift the velocity thresholds for negative-ion conversion to larger values. A comparison of the two cases indicates that for commensurate Z distances [see $Z = 3.0$ a.u. for F^0_{gas}-LiF and $Z = 3.5$ a.u. for F^0_{gas}-KI(100) in Figs. 7(b) and 7(d)], the onset of negative-ion conversion occurred at smaller velocity values in F^0_{gas}-KI(100) than in F^0_{gas}-LiF(100).

C. Comparison of the theoretical and experimental results

The negative-ion fraction $P(N)$ for an incident beam crossing N rows of surface crystal ions obeys the first-order linear nonhomogeneous differential equation $dP(N)/dN = [1 - P(N)]P^{row}_{sin}(Z,v)$. The initial condition $P(N = 0) = 0$ is for neutral-projectile incidence. Thus, the final negative-ion fraction is $P(N) = 1 - \exp[-P^{row}_{sin}(Z,v)N]$. From Ref. [12], the important turning-point region for both studied cases was 2.0 a.u. $\leqslant Z_{tp} \leqslant$ 4.0 a.u., because the negative ions were mainly formed near the trajectory turning point. Therefore, as in Ref. [11], we chose $Z \approx 3.0$ a.u. ($Z \approx 2.8$ a.u. [19]) for F^0_{gas}-LiF(100) and $Z \approx 3.5$ a.u. for F^0_{gas}-KI(100). In addition, combining the computed $P^{row}_{sin}(Z,v) = \frac{1}{2}P^{site}_{sin}(Z,v)$, the final negative-ion conversion probabilities of the F^0 atoms after grazing scattering from the LiF(100) and KI(100) surfaces were calculated and are displayed in Figs. 8(a) (blue solid line) and 8(b) (red solid line), along with the experimental data from Ref. [11]. As can be observed from the figures, for large velocities the previous theoretical results saturated [see Figs. 8(a) and 8(b)], whereas the experimentally measured negative-ion yield decreased. This poor agreement was attributed to the lack of accounting for the crucial electron-loss process, which resulted in destruction of negative ions at high velocities. A crucial difference between previous approaches and this work is that the present approach incorporates the decrease in the electron affinity caused by Coulomb barrier tunneling loss to the vacuum. Therefore, our approach reproduces the whole velocity range of the experimental data, including the velocity thresholds for the negative-ion formation (particularly the large-velocity falloff), quite well.

The experimental data for F^- formation at a KI(100) surface show saturation of the negative-ion fraction, as predicted by

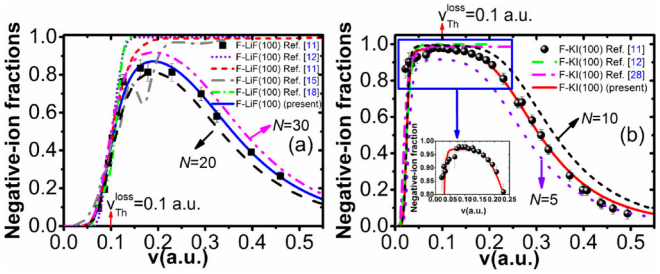

FIG. 8. (a) Comparison of the negative-ion yield with projectile velocity as measured for F^0_{gas}-LiF(100) in Ref. [11] for an incidence angle $\alpha \approx 1^\circ$ (data points) with the present computation (blue solid line). Previous theoretical results: *ab initio* quantum chemistry parameter-free calculation of Ref. [12] (violet dotted line); simple model with the adjustable-parameter fit of Ref. [11] (red short-dashed line); Hartree-Fock Roothaan calculation of Ref. [15] (gray dash-dotted line); coupled-cluster calculation of Ref. [19] (green short-dash–dotted line). (b) Comparison of the negative-ion yield with projectile velocity measured for F^0_{gas}-KI(100) in Ref. [11] for an incidence angle $\alpha \approx 1^\circ$ (data points) with the present computation (red solid line). Previous theoretical results: *ab initio* quantum chemistry parameter-free calculation of Ref. [12] (green dashed line); simple model with the adjustable-parameter fit of Ref. [28] (magenta dash-dotted line).

the present approach [Fig. 8(b) and inset]. This saturation is attributed to the very efficient electron capture by the projectile from $I^-_{\text{active site}}$ at low velocities of $v < v^{\text{loss}}_{\text{Th}}$ [see Figs. 7(c) and 7(d)], where practically no loss occurred [see Fig. 6(b)]. Coulomb repulsive barrier tunneling significantly reduced the electron affinity and thus led to an efficient F^- destruction threshold of $v^{\text{loss}}_{\text{Th}} \approx 0.1$ a.u. [see Figs. 8(a) and 8(b), red arrows]. For F^- formation at an LiF(100) surface, the requirement of a comparatively much greater velocity [$v \geqslant 0.05$ a.u.; see Fig. 8(a)] resulted in the observed velocity regions for electron capture and substantial loss of overlap. Therefore, no saturation of the F^- fraction was observed in this case [Fig. 8(a)].

The more efficient negative-ion formation in F^0_{gas}-KI(100) than in F^0_{gas}-LiF(100) clearly resulted from the small energy difference $\Delta E_{\text{ave}}(Z,v)$ [Figs. 5(c) and 5(d)] in F^0_{gas}-KI(100), which led to a remarkably large single-collision negative-ion conversion probability $P^{\text{site}}_{\text{sin}}(Z,v)$ [see Figs. 7(c) and 7(d)].

The rapid increase in the negative-ion fraction after the threshold was due not only to the velocity dependence of the binary-collision negative-ion conversion probability $P^{\text{site}}_{\text{sin}}(Z,v)$ observed in Figs. 7(a)–7(d), but also to the increase in the effective projectile-beam crossing number N with increasing projectile velocity; after the expression of the final negative-ion fraction above, the negative-ion formation probability rapidly increased with N. To clearly show this influence, we presented the results of $N_{\text{LiF}} = 20, 30$ and $N_{\text{KI}} = 5, 10$ in Figs. 8(a) and 8(b). It is beyond the scope of the present work to accurately determine the projectile-beam crossing number N [used to calculate the cumulative electron-transfer probability $P^{\text{row}}_{\text{sin}}(Z,v)$] (which is closely related to the projectile trajectory calculation). Moreover, despite the attempts by Borisov *et al.* [15] to estimate the effective crossing number by $N \approx 2d/(a \tan\alpha)$, the number is unavailable because of the failure to determine d, where d represents the range from the distance of closest approach to the surface within which the trajectories contribute most. A typical conservative estimate is $d < 2$ a.u.; hence, $N_{\text{LiF}} < 30$ and $N_{\text{KI}} < 17$. Here, for F^0_{gas}-LiF(100) and KI(100) in Figs. 8(a) and 8(b), $N_{\text{LiF}} = 25$ and $N_{\text{KI}} = 7$, respectively. Note that because of the inclusion of the important image interaction $U_{\text{image}}(Z,v)$ reduction (which also introduces a velocity dependence) in the energy defect ΔE, the values of the parameter N for LiF and KI are different from those reported in Ref. [28]. Those values were $N_{\text{LiF}} = 20$ and $N_{\text{KI}} = 10$, where the energy defect was fixed at $\Delta E = 3.5$ eV and 0.5 eV for F^0-LiF(100) and F^0-KI(100) respectively, as estimated from the projectile trajectory calculated from binary potentials of $N_{\text{LiF}} = 30$ for fixed energy defect at $\Delta E_{F^-} = 3.0$ eV [11]. For both studied systems, the large difference in the values of N (present values, $N_{\text{LiF}} \approx 3.6 N_{\text{KI}}$) may result from the smaller $P^{\text{site}}_{\text{sin}}(Z,v)$ of $F^0_{gas} + F^-_{\text{active site}} \rightarrow F^-_{gas} + F^0_{\text{active site}}$ [Figs. 7(a) and 7(b)] than that of $F^0_{gas} + I^-_{\text{active site}} \rightarrow F^-_{gas} + I^0_{\text{active site}}$ [Figs. 7(b) and 7(d)].

V. CONCLUSIONS

We considered the evolution of the charge state of a neutral projectile in grazing scattering from alkali-metal-halide crystal surfaces. The final charge fractions in the scattered beam were governed by (1) capture of the electron from the valence band of the surface halogen sites to the projectile affinity and (2) the survival of the resulting negative ion from the possible destruction channels. Here, the crucial decrease in the electron affinity caused by Coulomb barrier tunneling to the vacuum level near the surface anion sites was treated. According to the localization of the valence-band electrons at the negatively charged (halogen) sites, and taking into account both key effects—ML polarization and image interactions in electron capture—we proposed a general approach to address the problem of the complete velocity range of negative-ion conversion in grazing scattering of neutral projectiles from AB-type ionic crystal (alkali-metal halides, oxides) surfaces. The approach attributes the buildup of the charge state in the scattered beam to a series of binary electron-transfer processes between the projectiles and the negatively charged surface sites.

As an application of this approach, we studied F^- formation in grazing collisions of F atoms with LiF(100) and KI(100) surfaces. Our results clearly imply that electron transfer is indeed localized at the negatively charged halogen (F^- or I^-) sites on the surfaces.

The present calculation offers a good description of the different features observed in the experimental F^- yields in the complete velocity region, such as the experimentally observed velocity thresholds, the rapid increase in the negative-ion yields above this threshold, the related saturation [see Fig. 8(b) and inset], and the decrease in the large-velocity negative-ion yields. Moreover, pronounced differences in the efficiency of F^- formation at the LiF(100) and KI(100) surfaces can also be interpreted well using our approach.

Note that the ML-polarization and image interactions directly reduce the electron-capture energy defect, in addition to the influence of the lattice constant on the energy defect.

This shows that, for an ionic crystal with large anion and cation polarizations, a large image interaction and a large lattice constant will significantly improve the single-collision negative-ion conversion probability, thereby increasing the final negative-ion conversion efficiency of neutral atoms.

Finally, to further reveal the possible electron-loss channels, additional studies are required to disentangle the existence of the dynamically assisted electron loss regarding conduction-band and lattice-period field stripping processes.

ACKNOWLEDGMENTS

We thank Dr. Huanwang Jing for helpful discussions. This work is financially supported by the National Natural Science Foundation of China (Grant Nos. 11175075, 11404152).

[1] *Nanotechnology for Electronic Materials and Devices*, edited by A. Korkin, E. Gusev, J. K. Labanowski, and S. Luryi (Springer, New York, 2007).
[2] K. J. Stout and L. Blunt, *Three-Dimensional Surface Topography* (Penton Press, London, 2000).
[3] S. A. Campbell, *The Science and Engineering of Microelectronic Fabrication* (Oxford University Press, New York, 2001).
[4] J. W. Rabalais, *Principles and Applications of Ion Scattering Spectrometry: Surface Chemical and Structural Analysis* (Wiley-Interscience, Hoboken, NJ, 2003).
[5] A. G. Borisov, D. Teillet-Billy, J. P. Gauyacq, H. Winter and G. Dierkes, Phys. Rev. B **54**, 17166 (1996); M. Maazouz, A. G. Borisov, V. A. Esaulov, J. P. Gauyacq, L. Guillemot, S. Lacombe, and D. Teillet-Billy, *ibid.* **55**, 13869 (1997).
[6] J. E. Miraglia, Phys. Rev. A **90**, 062715 (2014).
[7] B. Solleder, L.Wirtz, and J. Burgdörfer, Phys. Rev. B **79**, 125107 (2009).
[8] S. N. Markin, D. Primetzhofer, and P. Bauer, Phys. Rev. Lett. **103**, 113201 (2009).
[9] A. S. El-Said, R. Heller, W. Meissl, R. Ritter, S. Facsko, C. Lemell, B. Solleder, I. C. Gebeshuber, G. Betz, M. Toulemonde, W. Moller, J. Burgdorfer, and F. Aumayr, Phys. Rev. Lett. **100**, 237601 (2008).
[10] H. Zhou, L. Chen, D. Feng, Y. L.Guo, M. C. Ji, G. Y. Wang, W. Zhou, Y. Li, L. Zhao, and X. M. Chen, Phys. Rev. A **85**, 014901 (2012).
[11] C. Auth, A. Mertens, H. Winter, A. G. Borisov, and V. Sidis, Phys. Rev. A **57**, 351 (1998).
[12] A. G. Borisov and V. Sidis, Phys. Rev. B **56**, 10628 (1997).
[13] C. Auth, A. G. Borisov, and H. Winter, Phys. Rev. Lett. **75**, 2292 (1995).
[14] A. B. Kunz, Phys. Rev. B **12**, 5890 (1975); A. Zunger and A. J. Freeman, *ibid.* **16**, 2901 (1977); H. Tatewaki and E. Miyoshi, Surf. Sci. **327**, 129 (1995); G. K.Wertheim, J. E. Rowe, D. N. E. Buchanan, and P. H. Citrin, Phys. Rev. B **51**, 13675 (1995).
[15] A. G. Borisov, V. Sidis, and H. Winter, Phys. Rev. Lett. **77**, 1893 (1996).
[16] Dulal C. Ghosh and Raka Biswas, Int. J. Mol. Sci. **3**, 87 (2002).
[17] A. G. Borisov and V. A. Esaulov, J. Phys.: Condens. Matter **12**, R177 (2000).
[18] N. F. Mott and M. J. Littleton, Trans. Faraday Soc. **34**, 485 (1938); W. Beall Fowler, Phys. Rev. **151**, 657 (1966); G. D. Mahan, Phys. Rev. B **21**, 4791 (1980).
[19] A. G. Borisov, J. P. Gauyacq, V. Sidis, and A. K. Kazansky, Phys. Rev. B **63**, 045407 (2001).
[20] S. A. Deutscher, A. G. Borisov, and V. Sidis, Phys. Rev. A **59**, 4446 (1999).
[21] J. R. Tessman and A. H. Kahn, Phys. Rev. **92**, 890 (1953).
[22] P. M. Echenique and A. Howie, Ultramicroscopy **16**, 269 (1985); N. R. Arista, Phys. Rev. A **49**, 1885 (1994).
[23] E. D. Palik and W. R. Hunter, *Handbook of Optical Constants of Solids* (Academic Press, New York, 1985).
[24] L. D. Landau, Phys. Z. Sowjetunion **2**, 46 (1932); C. Zener, Proc. R. Soc. London, Ser. A **137**, 696 (1932).
[25] A. G. Borisov and J. P. Gauyacq, Phys. Rev. B **62**, 4265 (2000).
[26] J. M. Rost, Phys. Rev. Lett. **82**, 1652 (1999).
[27] L. D. Landau and E. M. Lifshitz, *Quantum Mechanics (Nonrelativistic Theory)*, 3rd ed. (reprinted by Beijing World Publishing Corporation by arrangement with Butterworth-Heinemann, Oxford, 1999), p. 182.
[28] H. Winter, A. Mertens, C. Auth, and A. G. Borisov, Phys. Rev. A **54**, 2486 (1996).